

Wideband Josephson Parametric Isolator

M. A. Beck,^{*} M. Selvanayagam, A. Carniol, S. Cairns, and C. P. Mancini
IBM Quantum, IBM T.J. Watson Research Center, Yorktown Heights, NY 10598, USA

(Dated: December 19, 2022)

The cryogenic hardware needed to build a superconducting qubit based quantum computer requires a variety of microwave components including microwave couplers, filters, amplifiers, and circulators/isolators. Traditionally, these are implemented via discrete components inserted in to the signal path. As qubit counts climb over the 100+ mark, the integration of these peripheral components, in an effort to reduce overall footprint, thermal load, and added noise in the overall system, is a key challenge to scaling. Ferrite-based microwave isolators are one of the physically largest devices that continue to remain as discrete components. They are generally employed in the readout chain to protect qubits and resonators from broadband noise and unwanted signals emanating from downstream components such as amplifiers. Here we present an alternative two-port isolating integrated circuit derived from the DC Superconducting Quantum Interference Device (DC-SQUID). The non-reciprocal transmission is achieved using the three-wave microwave mixing properties of a flux-modulated DC-SQUID. We show experimentally that, when multiple DC-SQUIDs are embedded in a multi-pole admittance inverting filter structure, RF flux pumping of the DC-SQUIDs can provide directional microwave power flow. For a three-pole filter device, we experimentally demonstrate a directionality greater than 15 dB over a 600 MHz bandwidth.

I. INTRODUCTION

Readout of superconducting quantum processing units (QPU's) is generally performed by dispersively coupling linear microwave resonators to individual qubits [1–3]. Determination of the qubit states is achieved via the application of a weak ($P \sim -120$ dBm) microwave probe tone to the linear resonator where the qubit state is mapped to a phase shift of the probe tone. This probe tone and its corresponding phase shift is then amplified, demodulated, and digitized at room temperature.

In many state-of-the-art QPU designs, multiplexed readout of multiple resonators is achieved via a common coupled transmission line [3–5]. This multiplexed readout scheme requires the resonators in the QPU to be decoupled from the downstream amplifiers and electronics over the entirety of the readout frequency band. In-band noise or signals emanating back towards the QPU from downstream readout electronics can introduce spurious photon populations to the quantum readout resonators leading to excess dephasing [6, 7]. Modern systems generally decouple the QPU from downstream electronics noise via commercial ferrite-based cryogenic microwave isolators. Modern single junction isolators generally achieve better than 20+ dB level of in-band isolation. Modern systems serially cascade multiples of these devices in effort to increase the overall isolation and thus prevent degradation of QPU performance.

As a consequence of their bulky construction, placing a large numbers of isolators at the mixing chamber of a dilution refrigerator to support increasing qubit counts is a daunting system integration challenge. In effort to meet the future demands of larger quantum systems, integrated circuit approaches towards realizing an isolator

replacement is an active area of research [8]. Recently, the inherent non-linear inductance of Josephson junctions (JJs) has been utilized to realize non-reciprocal behaviour [9]. Numerous JJ-based devices have been proposed building off of existing amplifier designs including non-reciprocal devices derived from JPA's [10], JRM's [11–13], and travelling wave devices [14, 15]. In addition, robust theoretical models of non-reciprocal time-varying Josephson junction based circuits have been developed based on multi-mode modelling and graph theory [16, 17].

We propose a two-port circuit that incorporates multiple DC-SQUID's in effort to achieve non-reciprocal transmission as a key building block towards the realization of a broadband ferrite-based isolator replacement. By utilizing a band-pass filter structure to embed the DC-SQUIDS, the device remains matched at either port while demonstrating broadband non-reciprocal transmission. In this work, we discuss a theoretical model based on a multi-modal spectral matrix treatment of the DC-SQUID non-linearity, the design and operation of the circuit, and comparison of experimental data to numerical simulations of the devices. We also show experimental data detailing the potential for directional amplification and achieving higher levels of non-reciprocity via the serial cascading of these devices.

II. CIRCUIT IMPLEMENTATION

A. DC-SQUID Mixer Theory

A DC-SQUID is comprised of the parallel combination of two Josephson junctions in a superconducting loop [18]. The DC-SQUID possesses an inherent inductance with a non-linear dependence on the applied flux through

^{*} matthew.beck@ibm.com

the loop. The form of the inductance is:

$$L_{SQ} = \frac{\Phi_0}{2\pi I_c \cos(\pi\Phi_A/\Phi_0)}, \quad (1)$$

where $\Phi_0 \equiv h/2e$ is the superconducting magnetic flux quantum, $I_c \equiv 2 \times I_{c0}$ is twice the critical current (I_{c0}) of the individual JJs, and Φ_A is the applied flux through the DC-SQUID loop. In the limit of $\Phi_A \ll \Phi_0$, a second order Taylor expansion of Eq. (1) yields

$$L_{SQ} \approx \frac{\Phi_0}{4\pi I_{c0}} \left(1 + \pi^2 \Phi_A^2 / \Phi_0^2\right). \quad (2)$$

Taking $\Phi_A/\Phi_0 = \beta + \alpha \cos(\omega_m t + \phi)$ where $\beta = \Phi_{DC}/\Phi_0$ and $\alpha = \Phi_{RF}/\Phi_0$ are the DC and RF flux amplitudes, respectively and ω_m and ϕ are the frequency and phase of the RF flux drive, Eq. (2) can be expanded to

$$L_{SQ}(t) \approx \frac{\Phi_0}{4\pi I_{c0}} \left[1 + \frac{\pi^2 \beta^2}{2} + \frac{\pi^2 \alpha^2}{4} + \frac{\pi^2 \alpha^2}{8} (e^{i2\omega_m t + i2\phi} + e^{-i2\omega_m t - i2\phi}) + \frac{\pi^2 \alpha \beta}{2} (e^{i\omega_m t + i\phi} + e^{-i\omega_m t - i\phi}) \right]. \quad (3)$$

The first three terms are the bare, DC modulated, and RF modulated terms of the SQUID inductance, respectively. The fourth and fifth terms, whose amplitude depend solely on the normalized RF drive strength α , give rise to four-wave mixing which take $\omega \rightarrow \omega \pm 2\omega_m$. The final two terms which depend on *both* the normalized DC and RF drive strengths β and α provide three-wave mixing which takes $\omega \rightarrow \omega \pm \omega_m$. Depending on the frequency of the RF modulation with respect to a signal tone applied to the DC-SQUID's terminals, these modulating tones can drive either amplification or frequency conversion processes. For the application in question we will focus mainly on frequency conversion processes but note that this derivation can be generalized to either.

Given the form of Eq. (3), one can write the voltage/current relationship of a DC-SQUID as

$$V(t) = L_{SQ}(t) \frac{dI(t)}{dt}, \quad (4)$$

where we have taken the current to be of the form $I(t) = I_0 \exp[i\omega' t]$. Taking the Fourier Transform \mathcal{F} of both sides results in

$$\mathcal{F}\{V(t)\} = i\omega' \mathcal{F}\{L_{SQ}(t)\} * \mathcal{F}\{I(t)\}. \quad (5)$$

This results in a frequency domain voltage/current relationship given by

$$V(\omega) = L_{SQ}^0 [\gamma \delta(\omega' - \omega) + \eta_+ \delta(\omega' - \omega + 2\omega_m) + \eta_- \delta(\omega' - \omega - 2\omega_m) + \kappa_+ \delta(\omega' - \omega + \omega_m) + \kappa_- \delta(\omega' - \omega - \omega_m)] * i\omega' I(\omega'), \quad (6a)$$

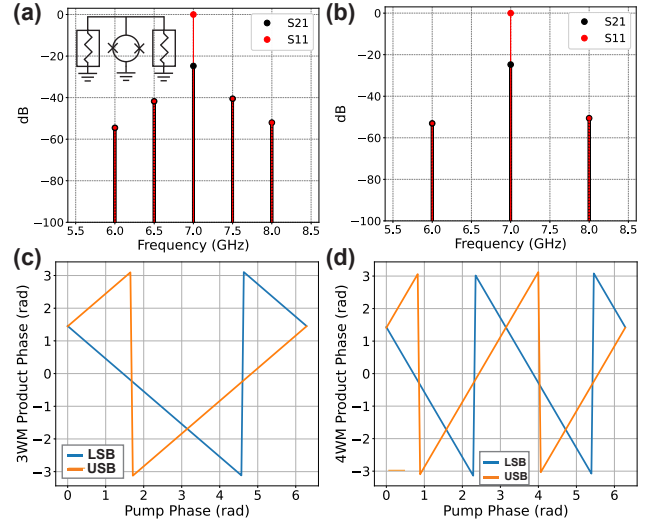


FIG. 1. (color online) (a) The forward and reflected scattering spectrums for a DC+RF flux biased DC-SQUID with $\alpha = \beta = 0.2$. (inset) Circuit diagram for 2-port DC-SQUID calculation. (b) Forward and reflected scattering spectrum for a RF flux biased DC SQUID with $\alpha = 0.2$. (c) The transmitted phase for the first 3WM upper and lower sideband as a function of RF Flux pump phase. (d) The transmitted phase for the first 4WM upper and lower sideband as a function of RF pump phase.

$$V(\omega) = i\omega L_{SQ}^0 \gamma I(\omega) + i[\omega + 2\omega_m] L_{SQ}^0 \eta_+ I(\omega + 2\omega_m) + i[\omega - 2\omega_m] L_{SQ}^0 \eta_- I(\omega - 2\omega_m) + i[\omega + \omega_m] L_{SQ}^0 \kappa_+ I(\omega + \omega_m) + i[\omega - \omega_m] L_{SQ}^0 \kappa_- I(\omega - \omega_m), \quad (6b)$$

where $L_{SQ}^0 = \Phi_0/4\pi I_{c0}$, $\gamma = 1 + \pi^2 \beta^2/2 + \pi^2 \alpha^2/4$, $\eta_{\pm} = \pi^2 \alpha^2 e^{\pm i2\phi}/8$, and $\kappa_{\pm} = \pi^2 \alpha \beta e^{\pm i\phi}/2$. The Dirac delta functions in Eq. (6a) form the connection between the signal and the sidebands produced from the mixing terms. From this, we can formulate the DC-SQUID spectral impedance matrix \mathbf{Z}_{SQ} where the voltage, current, and impedance are defined to account for $\pm 2\omega_m$ and $\pm \omega_m$ modulation products resulting from the Taylor expansion of Eq. (2).

$$\begin{bmatrix} V(\omega - 2\omega_m) \\ V(\omega - \omega_m) \\ V(\omega) \\ V(\omega + \omega_m) \\ V(\omega + 2\omega_m) \end{bmatrix} = \mathbf{Z}_{SQ}(\omega) \begin{bmatrix} I(\omega - 2\omega_m) \\ I(\omega - \omega_m) \\ I(\omega) \\ I(\omega + \omega_m) \\ I(\omega + 2\omega_m) \end{bmatrix} \quad (7)$$

Equation (8) gives the spectral impedance matrix $\mathbf{Z}_{SQ}(\omega)$ for a single DC-SQUID [19]. Crucially, Eq. (8) demonstrates that the conversion amplitudes and associated phases between modulation products are *asymmetric* with respect to the conversion from one sideband to another. Embedding multiple DC-SQUIDS in a two-port

$$\mathbf{Z}_{\text{SQ}}(\omega) = iL_{\text{SQ}}^0 \begin{bmatrix} \gamma[\omega - 2\omega_m] & \kappa_-[\omega - 2\omega_m] & \eta_-[\omega - 2\omega_m] & 0 & 0 \\ \kappa_+[\omega - \omega_m] & \gamma[\omega - \omega_m] & \kappa_-[\omega - \omega_m] & \eta_-[\omega - \omega_m] & 0 \\ \eta_+\omega & \kappa_+\omega & \gamma\omega & \kappa_-\omega & \eta_-\omega \\ 0 & \eta_+[\omega + \omega_m] & \kappa_+[\omega + \omega_m] & \gamma[\omega + \omega_m] & \kappa_-[\omega + \omega_m] \\ 0 & 0 & \eta_+[\omega + 2\omega_m] & \kappa_+[\omega + 2\omega_m] & \gamma[\omega + 2\omega_m] \end{bmatrix} \quad (8)$$

system and then tuning these pump phases will be key to providing asymmetric transmission between the ports.

B. Two-Port S-parameters of a DC-SQUID

With the multi-mode impedance matrix for a DC-SQUID now defined, the scattering parameters of a shunted DC-SQUID can be calculated. The basic circuit is illustrated in the inset of Fig. 1(a) where a DC-SQUID under RF modulation is shunted to ground between two physical ports. The spectral **ABCD** matrix for a shunt DC-SQUID is defined to be

$$\overline{\mathbf{M}}_{\text{SQ}} \equiv \begin{bmatrix} \mathbf{A} & \mathbf{B} \\ \mathbf{C} & \mathbf{D} \end{bmatrix} = \begin{bmatrix} \mathbf{I}_n & \mathbf{0}_n \\ \mathbf{Z}_{\text{SQ}}^{-1}(\omega) & \mathbf{I}_n \end{bmatrix}, \quad (9)$$

where \mathbf{I}_n is the $n \times n$ identity matrix and $\mathbf{0}_n$ is a $n \times n$ matrix comprised of all zeroes. The resulting S-parameters are then given by [8, 20]

$$\mathbf{S}_{11} = \mathbf{I}_n - 2[\mathbf{I}_n + (\mathbf{AZ}_0 + \mathbf{B})] \quad (10a)$$

$$\times (\mathbf{CZ}_0^2 + \mathbf{DZ}_0)^{-1}]^{-1}$$

$$\mathbf{S}_{21} = 2[\mathbf{A} + \mathbf{B}/Z_0 + \mathbf{CZ}_0 + \mathbf{D}] \quad (10b)$$

$$\mathbf{S}_{12} = 2[\mathbf{I}_n + (\mathbf{AZ}_0 + \mathbf{B})(\mathbf{CZ}_0 + \mathbf{D})^{-1}/Z_0] \quad (10c)$$

$$\times (\mathbf{A} - (\mathbf{AZ}_0 + \mathbf{B})(\mathbf{CZ}_0 + \mathbf{D})^{-1}\mathbf{C})$$

$$\mathbf{S}_{22} = \mathbf{I}_n - 2[\mathbf{I}_n + (\mathbf{AZ}_0 + \mathbf{CZ}_0^2)^{-1}] \quad (10d)$$

$$\times (\mathbf{B} + \mathbf{DZ}_0)^{-1},$$

where each entry in the respective spectral S-parameter matrix is defined as

$$S_{ij}^{np} = \frac{b_i(\omega + n\omega_m)}{a_j(\omega + p\omega_m)}. \quad (11a)$$

The terms b_i and a_j are the voltage waves entering and leaving each port at their respective frequencies defined by the indices n and p . Note that these S-parameter definitions are implicitly functions of the DC bias and RF modulation power applied to the DC-SQUID and require recalculation at every bias point. We note that this definition is similar to what is discussed in [21].

We calculate the S-parameters for a DC-SQUID modulated with at pump tone frequency $f_m = 500$ MHz with an RF signal tone $f_s = 7$ GHz. The critical current of the SQUID JJs is $I_{c0} = 5 \mu\text{A}$ and the RF amplitude $\alpha = 0.2$. Figures 1(a) and 1(b) display the calculated S-parameters in the three-wave ($\beta = 0.2$) and four-wave ($\beta = 0$) mixing cases, respectively.

Possessing solely a complex admittance, the DC-SQUID interrupts the impedance match between the ports. However, the three- and four-wave mixing processes are clearly evident in the spectrum of transmitted power. Figures 1(c) and 1(d) display the simulated first upper and lower sideband phases as a function of the modulation pump tone phase. For a single DC-SQUID, the forward \mathbf{S}_{21} and reverse \mathbf{S}_{12} scattering parameters are equal in magnitude. However, the transmitted and reflected sideband phases have a well-defined dependency on the phase of DC-SQUID RF modulation tone. It is this phase dependency that we aim to utilize in a multi-SQUID architecture to achieve directional power flow. To achieve this non-reciprocity over a broad frequency band, two conditions must be met: **(1)** Impedance match the SQUID over the desired frequency band and **(2)** Use multiple DC-SQUIDS to constructively and destructively interfere the modulation tones and generate asymmetric transmission at the signal tone.

C. Achieving Broadband Performance

To properly match the DC-SQUIDS, admittance inverting filter networks are employed [8, 22, 23]. For a defined filter type (e.g. Chebyshev, Bessel, etc.), number of filter poles, frequency bandwidth, and band-pass ripple, these filter networks can be constructed directly via conversion of low-pass prototype parameters [24]. Once the design of the filter is complete, the inclusion of the DC-SQUIDS is done via partial or full replacement of each LC pole's shunt inductor with the statically flux biased DC-SQUID equivalent.

III. FILTER RESPONSE CALCULATION

The calculation of the isolating filter response is performed via cascading of the ABCD matrix for each admittance inverter and subsequent shunt LC pole. For a two-pole device the equation takes the form

$$\begin{aligned} \overline{\mathbf{M}}_{2P} &= M_{J_{01}} M_{P1} M_{J_{12}} M_{P2} M_{J_{23}} \\ &= \begin{bmatrix} \frac{J_{23} \mathbf{Y}_{P1}}{iJ_{01} J_{12}} & \frac{\mathbf{Y}_{P1} \mathbf{Y}_{P2} + J_{12}^2 \mathbf{I}_n}{iJ_{01} J_{12} J_{23}} \\ \frac{J_{01} J_{23} \mathbf{I}_n}{iJ_{12}} & \frac{J_{01} \mathbf{Y}_{P2}}{iJ_{12} J_{23}} \end{bmatrix} \end{aligned} \quad (12)$$

where

$$M_{J_{XY}} = \begin{bmatrix} \mathbf{0}_n & -i\mathbf{I}_n/J_{XY} \\ -i\mathbf{I}_n J_{XY} & \mathbf{0}_n \end{bmatrix} \quad (13)$$

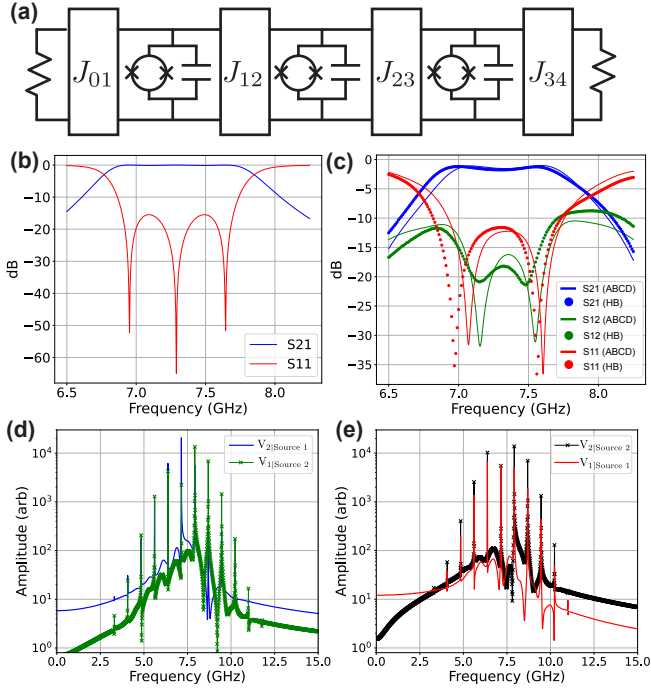


FIG. 2. (color online) (a) Three pole admittance inverting filter with DC-SQUIDs as shunt inductors. (b) ABCD matrix calculated filter response with DC flux applied to each SQUID with no RF modulation. (c) Comparison between the ABCD matrix calculation and harmonic balance simulation of the filter response with both DC bias and RF modulation of the DC-SQUIDs. With degenerate frequency RF pumps applied to each of the three SQUIDs, tuning of the discrete phase differences between them can produce asymmetric transmission $|S_{21}^{00}(\omega)| \neq |S_{12}^{00}(\omega)|$. An important characteristic of this design is that the filter stays matched with an in-band return loss greater than 10 dB. (d) Time domain simulated transmitted voltage for the circuit in (a) driven at 7.150 GHz. When driving port 1 and measuring at port 2 ($V_{2|\text{Source 1}}$), the energy remains in the central frequency peak while in the reverse operation ($V_{1|\text{Source 2}}$), the energy is dispersed into the three-wave mixing sidebands. (e) Time domain simulated reflected voltage spectrum of the circuit in (a) when driven at 7.150 GHz.

is the spectral ABCD matrix of the of the admittance inverter connecting poles X and Y and

$$\mathbf{Y}_{\text{PN}} = \mathbf{Y}_{\text{CN}} + \mathbf{Z}_{\text{SQ}, \text{N}}^{-1} \quad (14)$$

is the spectral admittance matrix of the N th pole. Using the same methodology, the three-pole ABCD matrix takes the form

$$\overline{\mathbf{M}}_{3\text{P}} = \begin{bmatrix} \frac{J_{34}J_{12}^2\mathbf{I}_n + J_{34}\overline{\mathbf{Y}}_{\text{P1}}\overline{\mathbf{Y}}_{\text{P2}}}{J_{01}J_{12}J_{23}} & \frac{J_{23}^2\overline{\mathbf{Y}}_{\text{P1}} + J_{23}^2\overline{\mathbf{Y}}_{\text{P3}} + \prod_{\alpha=1}^3 \overline{\mathbf{Y}}_{\text{Pa}}}{J_{12}J_{23}J_{34}} \\ \frac{J_{01}J_{34}\overline{\mathbf{Y}}_{\text{P2}}}{J_{12}J_{23}} & \frac{J_{01}J_{23}^2\mathbf{I}_n + J_{01}\overline{\mathbf{Y}}_{\text{P2}}\overline{\mathbf{Y}}_{\text{P3}}}{J_{12}J_{23}J_{34}} \end{bmatrix}. \quad (15)$$

We numerically calculate the response of a three-pole admittance inverting filter under both quiescent DC flux

bias and RF modulation conditions. We choose a Chebyshev filter response with center frequency $F_c = 7.3$ GHz, $\text{BW} = 800\text{MHz}$, and in-band ripple $r_{\text{dB}} = 0.125$ dB. The impedances of the three poles were set to 15, 10, and 15 Ohms, respectively. For these simulations, we focus on the $\pm\omega_m$ and $\pm 2\omega_m$ modulation products in addition to the signal tone resulting in 5×5 spectral S-parameter matrices. Furthermore, we replace the entirety of the linear shunt inductance with an equivalent flux biased DC-SQUID. Figure 2(a) displays a schematic of the simulated circuit. For no RF modulation and when properly biased at a value of $\beta = 0.3$, the ABCD matrix calculated response of the filter is that of a standard band-pass filter as displayed in Fig. 2(b).

We then calculate the circuit response again but now with each SQUID pumped at a common RF frequency and RF amplitude, but with differential phases. To verify our methodology, we compare our calculated results with that of a numerical harmonic balance simulation of the circuit. For the harmonic balance simulations, equivalent capacitive π -networks were utilized to implement the admittance inverters and a mathematically equivalent non-linear model of the DC-SQUID was implemented. To capture the full non-linearity of the circuit, 9 orders in the signal and pump frequencies were utilized. Figure 2(c) displays the overlaid results of both the spectral ABCD matrix calculation and the harmonic balance simulation. For the spectral ABCD matrix calculation, $\beta = 0.3$, $\alpha = 0.087$ and a pump frequency $f_m = 720$ MHz were used. The phases of the pumps were set to 0, $\pi/4$, and $\pi/2$, respectively. To achieve a matching response in the harmonic balance simulations, the pump frequency and RF pump amplitude had to be modified slightly to $f_m = 770$ MHz and $\alpha = 0.044$, respectively. This modification of the parameters to achieve a phenomenologically matching response is expected as in the ABCD calculation, the DC-SQUID non-linearity is only expanded to 2nd order. Higher orders of the applied flux $\mathcal{O}(\Phi_A^n)$ where $n > 2$ provide small but non-negligible alterations to the filter response that are more accurately captured in the harmonic balance simulations.

Figures 2(c) and 2(d) display time-domain simulation results for the reflected and transmitted voltage spectrums from the three-pole isolating filter with the signal frequency at 7.150 GHz. In the forward direction (drive port 1 and measure at port 2), the voltage is three-wave mixed from the carrier frequency and back resulting in constructive interference and near unity transmission. The additional insertion loss is due to the imperfect mode conversion back to the original signal frequency resulting in residual voltage in the sidebands. This residual voltage is then either reflected back out of port 1 (Fig. 2(e), red curve) or transmitted through to port 2. In the reverse direction (drive port 2 and measure at port 1), the power at the signal mode is three-wave mixed *out of band* of the filter and reflected back out port 2 (Fig 2(e) Black Curve). Due to the combination of the filter's finite roll-off and imperfect mode conversion, the achieved iso-

lation is not infinite, with residual voltage at the signal frequency remaining unconverted and thus transmitted to port 1 with subsequent sidebands (Fig. 2(d), green curve).

Overall, the asymmetric transmission ratio at the signal frequency $D \equiv |S_{21}^{00}|/|S_{12}^{00}|$ is maximized in the linear filter band. In general, the harmonic balance simulation and spectral S-parameter model show good agreement for both the transmitted and reflected S-parameters at the signal frequency. While the harmonic balance model captures a more detailed picture of the non-linear behaviour of the DC-SQUID, the good agreement shows that the physics of the circuit are well captured via the spectral S-parameter calculations demonstrating that the lowest order modes dominate the response of the circuit when under modulation. Another important aspect of the device simulations is that they show the device remains matched under RF modulation with an in-band return loss greater than 10 dB.

IV. DESIGN AND FABRICATION

We present two different circuit designs, utilizing two- and three-pole filter structures respectively, to demonstrate the asymmetric transmission described above. Each device employed 90-degree, $Z=50 \Omega$ transmission line admittance inverters interconnecting each pole. For each pole, a common DC-SQUID geometry was employed for all designs with a geometric inductance of 12.8 pH as extracted with InductEx [25]. For each pole, a portion of the geometric shunt inductance is replaced by its flux-biased DC-SQUID equivalent, the proportion of which was deliberately chosen to provide critical currents in excess of $I_c > 1 \mu\text{A}$ and to have nominally identical critical currents for each JJ in the design. The component parameters for the two devices are listed in Table I. Employing 90-degree transmission line admittance inverters naturally symmetrizes the filter circuits such that the outer poles of each filter have the same impedance and thus the same component values. For the two-pole design, each pole is degenerate in their respective component values while for the three-pole design, the first and third pole each employ the same component values thus allowing for the geometric inductance's and capacitance's of poles 1 (L_{g1}/C_{g1}) and pole 3 (L_{g3}/C_{g3}) to be equal.

The devices are fabricated utilizing a Nb tri-layer process with a critical current density $J_c = 6 \mu\text{A}/\mu\text{m}^2$ [26].

	$I_{c0}(\mu\text{A})$	β_l	$L_{g1}(\text{pH})$	$L_{g2}(\text{pH})$	$C_{g1}(\text{pF})$	$C_{g2}(\text{pF})$
Two-Pole	4	4.9E-2	9.79	9.79	5.1	5.1
Three-Pole	3.5	4.3E-2	119.5	34	2.17	3.5

TABLE I. Physical design parameters for the two- and three-pole isolating filters

The process is comprised of two superconducting metallic layers with an insulating dielectric layer. All layers are patterned atop a thermally oxidized Silicon substrate. The base Nb layer M0 serves as a ground plane for the circuit while the second niobium layer M1 allows for contact to the JJ counter electrode and additional on-chip wiring. A micrograph of the two-pole circuit is displayed in Fig. 3(a). Each DC-SQUID has its own independent flux bias line (bottom left / top right) allowing for the application of DC and RF flux signals. A zoomed micrograph of an individual filter pole is presented in Fig. 3(b). The lumped shunt capacitor hangs vertically downward while the shunt inductor plus DC-SQUID are vertical with respect to the horizontal transmission line.

V. MEASUREMENTS

The packaged devices were loaded in a dilution refrigerator and thermally sunk to the mixing chamber stage. The devices were placed within a cryogenic thru-reflect-line (TRL) setup using RF switches [27]. The TRL standards were implemented for coaxially de-embedding the cabling, attenuation, and amplification in-between the VNA and the DUT up to the devices SMA cables. Because of the type of connector (Arden TR multicoax) used to connect the device package, approximately 18" of residual coaxial cable (flexible 047 coaxial cable) at either port was unable to be de-embedded, along with the package PCB and wirebonds. All of these elements are thus included in the overall insertion and return loss of the measurements presented below.

As shown in Fig. 3(c), the RF input lines to the TRL setup were attenuated at the 4K and mixing chamber stages for a total of 66 dB of explicit attenuation at the input. The output amplification is provided via cryogenic low-noise amplifiers at the 4K stage cascaded with low-noise amplifiers at room-temperature. The flux biases are delivered via coaxial lines with 20 dB of attenuation at the 4K stage and low-pass filtering at the MXC stage to protect the device from out-of-band noise. The room-temperature based signals are generated via DC current sources (Yokogawa GS200) and an RF CW sources (Holzworth HS900A) combined via a bias-tee at room-temperature. The device was characterized by a PNA (Keysight N5242B).

A. Two-Pole Isolating Filter Response

The measured DC flux biased response of the filter with accompanying harmonic balance simulation results are displayed in Fig. 4(a). An additional 1.5 dB of insertion loss is seen in the data when compared to the simulation. We attribute this difference to the imperfect calibration of the sample whereby the reference planes of the two-port calibration were offset from that of the sample planes by the additional coaxial cable, PCB traces,

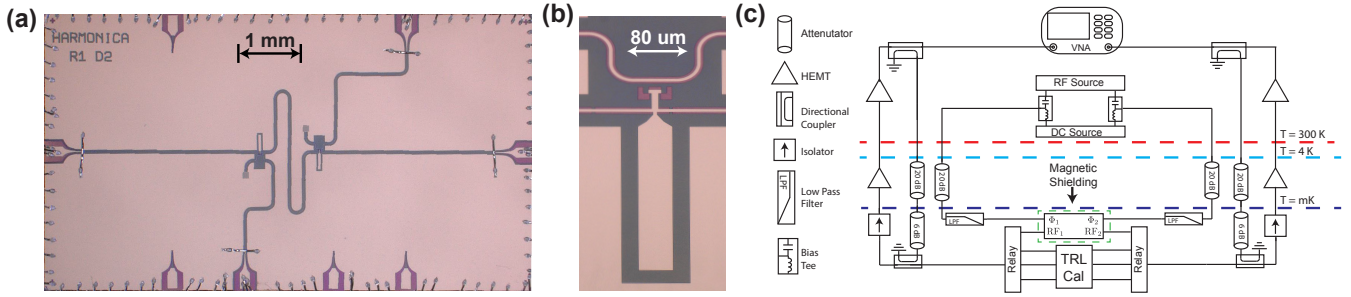


FIG. 3. (a) Micrograph of the two-pole device (b) Micrograph of a LC pole shunt capacitor and DC-SQUID. (c) Measurement wiring diagram of the two-pole device. The three-pole device measurement was performed with the same setup-up but with an additional pump line.

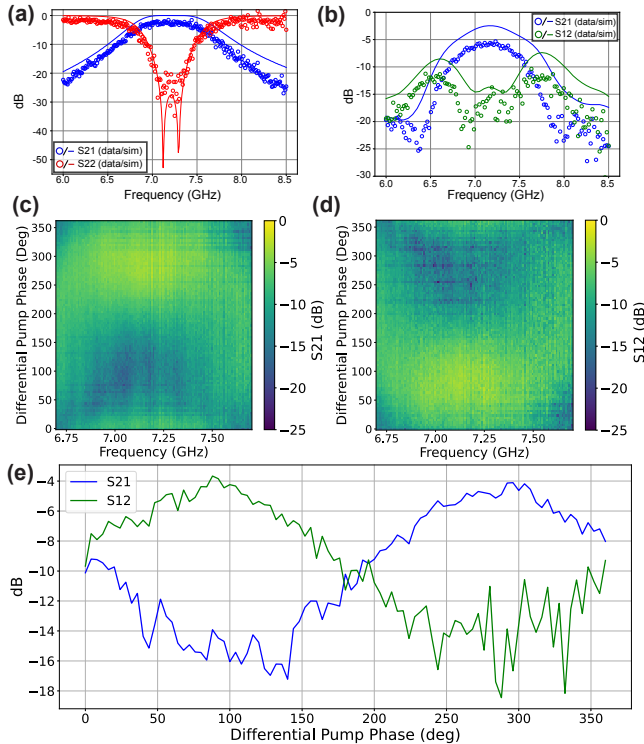


FIG. 4. (a) Simulated and measured response of the two-pole circuit at DC Flux bias. (b) Simulated and measured response of the two-pole circuit under differential RF modulation of the DC-SQUIDS. (c–d) S_{21}^{00} and S_{12}^{00} as a function of the differential pump phase and applied signal frequency. (e) Vertical line cuts of (c) and (d) at $f = 7.2$ GHz. The data shows that by adjusting the differential pump phase between the two DC-SQUIDS, the asymmetric transmission can be reversed from port 1 to 2 and vice versa.

and wirebonds at either RF port.

Despite this limitation, there is still excellent agreement between the simulation and measured data both in terms of bandwidth of the filter and the in-band return loss level.

The measured flux pumped response of the two-pole isolating filter is shown in Fig. 4(b) along with cor-

responding harmonic balance simulation of the device. The device is pumped at a frequency $f_m = 670$ MHz. Accounting for only the explicit attenuation in the flux line, the experimental flux amplitude α_E for the pump was $\alpha_E = 0.065$. The shown simulation results utilized a flux amplitude of $\alpha_S = 0.040$. Again we find excellent qualitative agreement between measurement and simulation. The difference in the max forward transmission between the measured and simulated response is ~ 3 dB. The majority of this discrepancy can again be explained by the additional insertion loss from the physically offset calibration planes. The additional ~ 1 dB of insertion loss seen while RF pumping we attribute to two factors. The first is inductance offsets arising from higher order RF pump amplitude terms which effects the impedance mismatches within the device. The second is loss in the dielectric of the parallel plate capacitors which is not included in the simulation model.

The phase offset between the two RF flux pumps in simulation was set to $\Delta\phi = 77.4^\circ$. Experimentally the absolute phase difference between the pumps at chip-level could not be determined due to differing electrical lengths between the independent pump channels. The appropriate phase offsets between the signals at room temperature was determined experimentally. Figures 4(c) and 4(d) display the measured forward and reverse scattering parameters of the two-pole device as a function of the differential phase offset. Figure 4(e) displays resulting vertical line cuts through 4(c) and 4(d) at $f = 7.2$ GHz. This data clearly shows that the direction of power flow in the device can be set by adjusting the differential phase offset between the pumps.

B. Three-Pole Isolating Filter Response

The measured response for the three-pole device under both quiescent DC flux bias and DC plus RF bias along with the corresponding harmonic balance simulations are displayed in figures 5(a) and 5(b), respectively. Referring to Fig. 5(a), we see excellent agreement between the harmonic balance simulation and the measured

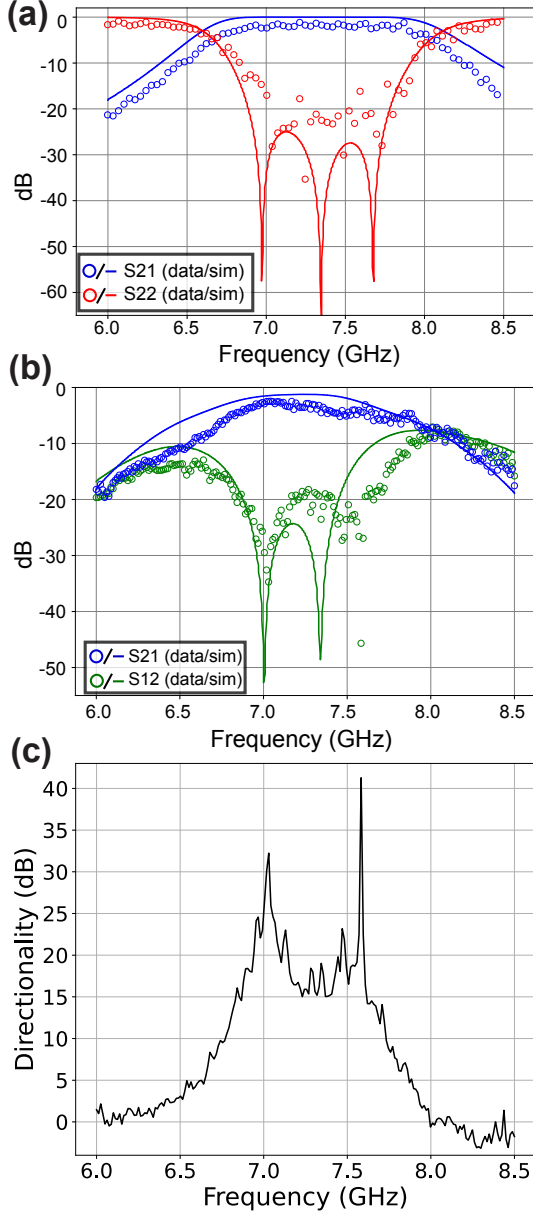


FIG. 5. (color online) (a) Measured and simulated response for a three-pole filter at optimized DC flux bias. (b) Measured and simulated 3 pole filter response when pumped at $f_p = 1036.5$ MHz with differing phases between pumps. The simulated response had differential phases between the three pumps of 0, 45.15, and 88.57 degrees, respectively. (c) Measured directionality $D = |S_{21}^{00}|/|S_{12}^{00}|$ of the three-pole isolating filter.

data at quiescent DC flux bias. There is ~ 1 dB discrepancy between the in-band through levels reported by the simulation and the measured data which we ascribe again to the imperfect calibration mentioned earlier. The RF pumped isolating filter response is displayed in Fig. 5(b). We apply a pump frequency $f_m = 1036.5$ MHz with an on-chip RF pump amplitude $\alpha_E = 0.056$. The simulated response was calculated with a RF pump amplitude

$\alpha_S = 0.0825$ with differential phases between the three pumps of 0, 45.15, and 88.57 degrees, respectively. Again the phase offsets required to produce the spectrum were found experimentally by independently sweeping individual pump phases at room temperature. When properly set, we experimentally realize an isolating band-pass filter with an insertion loss $IL < 5$ dB and a directionality $D > 15$ dB over a bandwidth $BW = 600$ MHz. The directionality D of the device is plotted in Fig. 5(c).

C. Directional Amplification

An independent mode of operation for the circuits described above is that of directional amplification. This mode is achieved by placing the pump frequency far above the center frequency of the pass band $f_m \gg f_c$. Setting $f_m = 2f_c$, the down converted terms in the upper-half of the impedance matrix in Equation (8) develop a negative and real amplitude yielding the potential for gain. The key to achieving gain directionality is again the provision of two or more pumps with different phases such that the amplified idler modes can be mixed back to the signal mode.

To probe this mode of operation, we apply pump tones of frequency $f_p = 14.69$ GHz to each SQUID of the three-pole device. The on-chip amplitude for each pump tone is calculated to be $\alpha_E = 0.099$. The resulting measured and simulated frequency response for S_{11}^{00} , S_{21}^{00} , and S_{12}^{00} are displayed in Fig. 6(a), 6(b), and 6(c), respectively. Referring to 6(a), both theory and measurement demonstrate that the device remains passive in reflection ($S_{11}^{00} < 0$) up to 7.3 GHz while showing gain in the forward direction, which is a different mode of operation than traditional reflection based amplifiers. With regards to the forward scattering parameter S_{21}^{00} , we measure greater than 5 dB of gain over a bandwidth of $BW \approx 700$ MHz with a peak gain of 15 dB at 7.25 GHz. Conversely, $S_{12}^{00} < 0$ dB up to approximately 7.4 GHz after which we begin to measure reverse amplification between 7.4–7.9 GHz with a maximum of 6 dB of gain at 7.7 GHz. In all

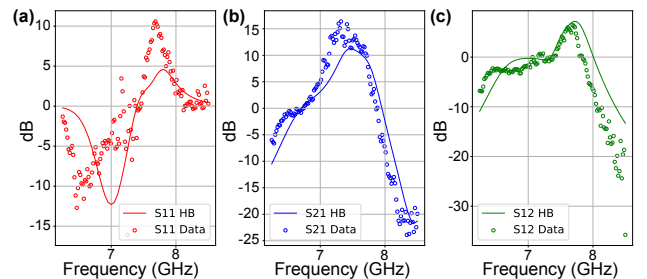


FIG. 6. (color online) (a) Measured and simulated S_{11}^{00} for the 3 pole device when pumped at 14.69 GHz. (b) Measured and simulated S_{21}^{00} for the 3 pole device when pumped at 14.69 GHz. (c) Measured and simulated S_{12}^{00} for the three-pole device when pumped at 14.69 GHz.

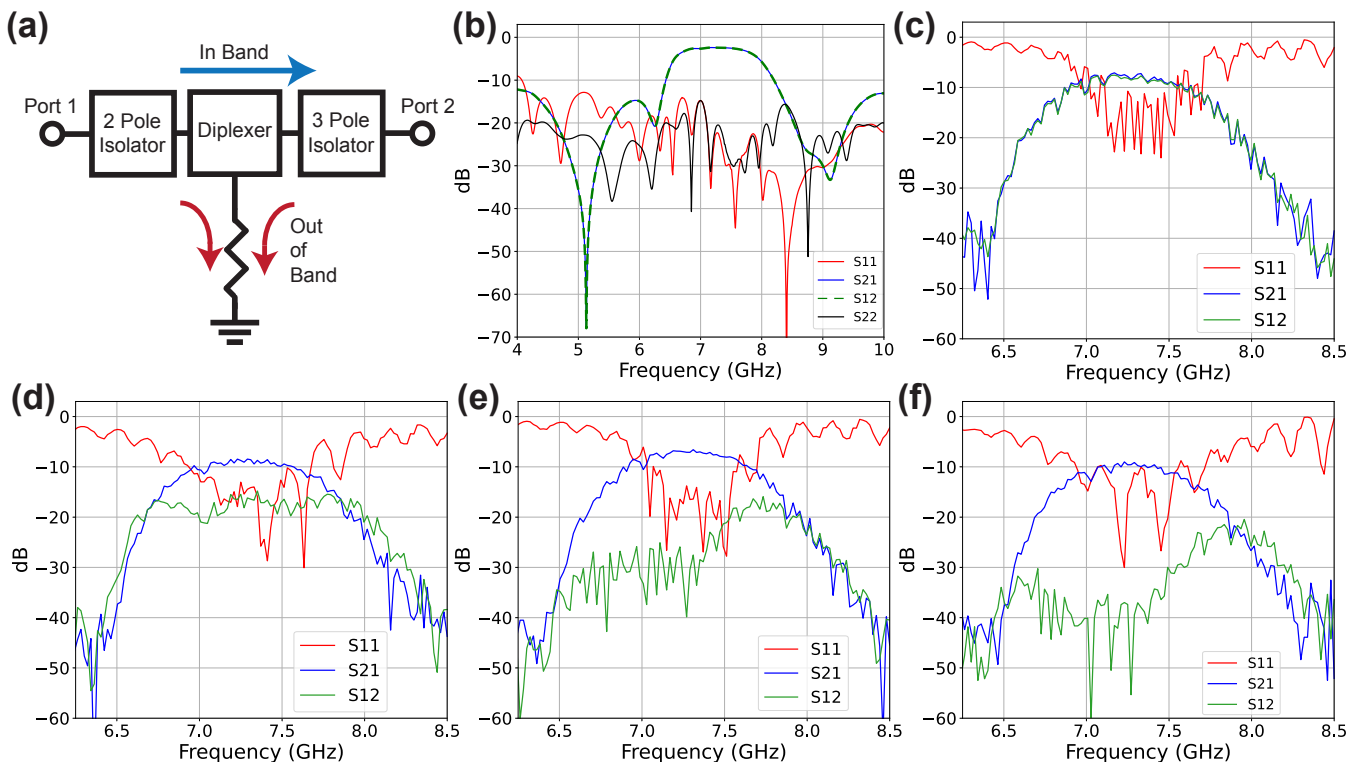


FIG. 7. (color online) (a) Circuit block diagram detailing how the isolator devices were cascaded. (b) Measured room temperature scattering parameters of the intermediate diplexer element at the ports used to connect the two isolator blocks. (c) DC flux tuned up cascaded isolators. The insertion loss of 8 dB is a combination of the insertion loss from the two filters and the diplexer plus an additional of 72 inches of microwave cable that could not be calibrated out of the measurement. (d) Cascaded isolator response with RF pumps applied solely to the two-pole device. (e) Cascaded isolator response with RF pumps applied solely to the three-pole device. (f) Cascaded isolator response with RF pumps applied to both the two and three-pole devices.

measured parameters, we see very good model–hardware correlation. To achieve a more ideal amplified filter response, further investigation is required to optimize the circuit parameters for this mode of operation.

D. Cascaded Filters

With the demonstration of the two- and three-pole isolating filters above, an obvious future path towards increasing the directionality for a set bandwidth is to increase the number of poles. While we leave that direction for future exploration, it is worth noting some of the difficulties with that approach. Specifically, moving to an $n > 3$ pole filter topology requires a more complicated device bring up and operation. Specifically, beyond just considering fabrication variation, this includes DC bias point optimization and static phase offsets at each DC-SQUID that must be optimized and maintained across the device.

A notable way to alleviate this complexity is to cascade two or more multi-pole devices in effort to achieve larger directionality. We highlight this approach for a few reasons. First, in comparison to building a more

complex circuit, the operation of two cascaded circuits can result in a simpler bring up. Each cascaded device can be brought up independently with respect to DC bias and pump phase offsets. With little to no interplay between the respective biases and pumps between devices, the requirements on the phases of the pumps are simpler to implement. Second, cascading parametric devices is a critical path to achieving tightly integrated, small footprint, readout electronics required for future quantum processors. Finally, in absence of large environmental offsets or fabrication variation, identical devices, once cascaded, ideally can share the same bias and pump lines significantly reducing wiring overhead.

To demonstrate this idea, we present data obtained from experiments on the previously characterized two- and three-pole devices cascaded in series with an intermediate microwave diplexer. The basic experimental setup for these experiments is shown in Fig. 7(a). The diplexer acts as an impedance match for the larger circuit across the full band of interest (including the stop-band under linear operation). The diplexer performs the function of filtering out and directing the sidebands that arise from either the two-pole or three-pole device while under modulation into a 50 ohm termination while simul-

taneously allowing the signals in the pass band to travel from port 1 to port 2. By filtering out harmonics between devices we prevent any unwanted standing waves and allow for each device to be treated as an independent circuit. The diplexer is constructed using discrete commercial off-the-shelf components (Krytar Hybrid Coupler 3060200, Mini-circuit filters, VLF-6000+ and VHF-8400+ and cryogenic 50-Ohm terminations from XMA Corporation). The diplexer's S-parameters, as measured at room temperature, are displayed in Fig. 7(b). We note that this passive circuit could be incorporated on-chip or on-package with small overhead in the overall design.

Fig. 7(c) displays the S-parameters for when both filters are biased with DC flux. The bandwidth of the pass-band is set by the two-pole filter. The best obtained insertion loss for the entire circuit was 8 dB. This insertion loss with respect to the calibration plane results from a combination of the insertion loss from the filters, diplexer, and an additional 72 inches of microwave cable required to wire the experiment due to the connectors on both devices (Arden TR multicoax). Both circuits were then tuned up independently for asymmetric transmission via application of RF flux to their respective LC poles. Fig. 7(d) displays the isolating filter response for when only the two-pole filter SQUIDs are pumped. The resulting directionality is $D \sim 8$ dB between 7.0–7.5 GHz. Fig. 7(e) displays the cascaded filter response with the RF pumps applied the the three-pole SQUIDs. A directionality of $D \sim 20$ dB is obtained with negligible insertion loss as compared to the non-pumped response. Finally, the data when both isolators are pumped is presented in Fig. 7(f). The additive effect of each filter's isolation is clearly seen in the suppression of the S12 over the band from 7.0–7.5 GHz, ultimately reaching a directionality in excess of 25 dB. Crucially, in all modes of

operation, the device remains matched in the band of interest with an in-band return loss greater than 10 dB. The ability to cascade these parametric devices, despite their non-linear mode of operation, allows for a straightforward method to incorporate these devices into a larger QPU readout chain.

VI. CONCLUSIONS

In summary, we have designed, modeled, and tested a new kind of two-port non-reciprocal device utilizing the three-wave mixing capabilities of DC-SQUIDs embedded in multi-pole admittance inverting filters. We developed a straightforward model that shows clearly how three- and four-wave mixing arises from the non-linear inductance of a DC-SQUID and can be utilized to realize non-reciprocal performance. This model was further verified via harmonic balance simulations where the full non-linearity of the SQUID inductance could be more properly captured. These models show excellent agreement with measured data taken on two- and three-pole isolator devices where we have achieved over a bandwidth of 500 MHz an in-band directionality of 8 and 15 dB, respectively. Further, we show with the three-pole device that directional amplification in excess of 10 dB over a 500 MHz BW can be achieved. Finally, we have presented measurements on the cascaded performance of a two- and three-pole isolating filter where a directionality approaching 30 dB was obtained with minimal added insertion loss from the RF pumps. These devices, with their straightforward design methodology, modeling, and fabrication, provide a path towards the replacement of commercial, ferrite-based microwave isolators with integrated circuits, with the ultimate goal of tighter peripheral hardware integration with quantum processors.

-
- [1] A. Wallraff, D. I. Schuster, A. Blais, L. Frunzio, J. Majer, M. H. Devoret, S. M. Girvin, and R. J. Schoelkopf. Approaching unit visibility for control of a superconducting qubit with dispersive readout. *Physical Review Letters*, 95(6):060501–, 08 2005.
- [2] Yu Chen, D. Sank, P. O'Malley, T. White, R. Barends, B. Chiaro, J. Kelly, E. Lucero, M. Mariantoni, A. Megrant, C. Neill, A. Vainsencher, J. Wenner, Y. Yin, A. N. Cleland, and John M. Martinis. Multiplexed dispersive readout of superconducting phase qubits. *Applied Physics Letters*, 101(18):182601, 2022/12/02 2012.
- [3] T. Walter, P. Kurpiers, S. Gasparinetti, P. Magnard, A. Potočnik, Y. Salathé, M. Pechal, M. Mondal, M. Oppliger, C. Eichler, and A. Wallraff. Rapid high-fidelity single-shot dispersive readout of superconducting qubits. *Phys. Rev. Applied*, 7:054020, May 2017.
- [4] C. Neill, P. Roushan, K. Kechedzhi, S. Boixo, S. V. Isakov, V. Smelyanskiy, A. Megrant, B. Chiaro, A. Dunsworth, K. Arya, R. Barends, B. Burkett, Y. Chen, Z. Chen, A. Fowler, B. Foxen, M. Giustina, R. Graff, E. Jeffrey, T. Huang, J. Kelly, P. Klimov, E. Lucero, J. Mutus, M. Neeley, C. Quintana, D. Sank, A. Vainsencher, J. Wenner, T. C. White, H. Neven, and J. M. Martinis. A blueprint for demonstrating quantum supremacy with superconducting qubits. *Science*, 360(6385):195–199, 2018.
- [5] Eric J. Zhang, Srikanth Srinivasan, Neereja Sundaresan, Daniela F. Bogorin, Yves Martin, Jared B. Hertzberg, John Timmerwilke, Emily J. Pritchett, Jeng-Bang Yau, Cindy Wang, William Landers, Eric P. Lewandowski, Adinath Narasgond, Sami Rosenblatt, George A. Keefe, Isaac Lauer, Mary Beth Rothwell, Douglas T. McClure, Oliver E. Dial, Jason S. Orcutt, Markus Brink, and Jerry M. Chow. High-performance superconducting quantum processors via laser annealing of transmon qubits. *Science Advances*, 8(19):eabi6690, 2022.
- [6] Maxime Boissonneault, J. M. Gambetta, and Alexandre Blais. Dispersive regime of circuit qed: Photon-dependent qubit dephasing and relaxation rates. *Physical Review A*, 79(1):013819–, 01 2009.

- [7] Eric I. Rosenthal, Christian M. F. Schneider, Maxime Malnou, Ziyi Zhao, Felix Leditzky, Benjamin J. Chapman, Waltraut Wustmann, Xizheng Ma, Daniel A. Palken, Maximilian F. Zanner, Leila R. Vale, Gene C. Hilton, Jiansong Gao, Graeme Smith, Gerhard Kirchmair, and K. W. Lehnert. Efficient and low-backaction quantum measurement using a chip-scale detector. *Physical Review Letters*, 126(9):090503–, 03 2021.
- [8] X. Wu, X. Liu, M. D. Hickle, D. Peroulis, J. S. Gómez-Díaz, and A. Álvarez Melcón. Isolating bandpass filters using time-modulated resonators. *IEEE Transactions on Microwave Theory and Techniques*, 67(6):2331–2345, 2019.
- [9] Leonardo Ranzani, Shlomi Kotler, Adam J. Sirois, Michael P. DeFeo, Manuel Castellanos-Beltran, Katarina Cicak, Leila R. Vale, and José Aumentado. Wideband isolation by frequency conversion in a josephson-junction transmission line. *Physical Review Applied*, 8(5):054035–, 11 2017.
- [10] F. Lecocq, L. Ranzani, G. A. Peterson, K. Cicak, R. W. Simmonds, J. D. Teufel, and J. Aumentado. Nonreciprocal microwave signal processing with a field-programmable josephson amplifier. *Physical Review Applied*, 7(2):024028–, 02 2017.
- [11] Baleegh Abdo, Nicholas T. Bronn, Oblesh Jinka, Salvatore Olivadese, Antonio D. Córcoles, Vivekananda P. Adiga, Markus Brink, Russell E. Lake, Xian Wu, David P. Pappas, and Jerry M. Chow. Active protection of a superconducting qubit with an interferometric josephson isolator. *Nature Communications*, 10(1):3154, 2019.
- [12] Baleegh Abdo, Oblesh Jinka, Nicholas T. Bronn, Salvatore Olivadese, and Markus Brink. High-fidelity qubit readout using interferometric directional josephson devices. *PRX Quantum*, 2:040360, Dec 2021.
- [13] T. C. Chien, O. Lanes, C. Liu, X. Cao, P. Lu, S. Motz, G. Liu, D. Pekker, and M. Hatridge. Multiparametric amplification and qubit measurement with a kerr-free josephson ring modulator. *Physical Review A*, 101(4):042336–, 04 2020.
- [14] Dengke Zhang and Jaw-Shen Tsai. Magnetic-free traveling-wave nonreciprocal superconducting microwave components. *Physical Review Applied*, 15(6):064013–, 06 2021.
- [15] Mahdi Naghiloo, Kaidong Peng, Yufeng Ye, Gregory Cunningham, and Kevin P. O’Brien. Broadband microwave isolation with adiabatic mode conversion in coupled superconducting transmission lines, 2021.
- [16] Leonardo Ranzani and José Aumentado. Graph-based analysis of nonreciprocity in coupled-mode systems. *New Journal of Physics*, 17(2):023024, 2015.
- [17] Ofer Naaman and José Aumentado. Synthesis of parametrically coupled networks. *PRX Quantum*, 3:020201, May 2022.
- [18] Robin Cantor and Dieter Koelle. *Practical DC SQUIDS: Configuration and Performance*, pages 171–217. Wiley-VCH, 2022/11/28 2004.
- [19] Kyle M. Sundqvist and Per Delsing. Negative-resistance models for parametrically flux-pumped superconducting quantum interference devices. *EPJ Quantum Technology*, 1(1):6, 2014.
- [20] J.A. Brandao Faria. *Multiconductor Transmission-Line Structures*. John Wiley and Sons, 1993.
- [21] Kaidong Peng, Rick Poore, Phillip Krantz, David E. Root, and Kevin P. O’Brien. X-parameter based design and simulation of josephson traveling-wave parametric amplifiers for quantum computing applications. *arXiv:2211.05328*, 2022.
- [22] O. Naaman, M. O. Abutaleb, C. Kirby, and M. Rennie. On-chip josephson junction microwave switch. *Applied Physics Letters*, 108(11):112601, 2022/12/02 2016.
- [23] David M. Pozar. *Microwave Engineering*. John Wiley and Sons, Inc., 3rd edition, 2005.
- [24] George Matthaei, Leo Young, and E.M.T Jones. *Microwave Filters, Impedance-Matching Networks, and Coupling Structures*. Artech House, 1980.
- [25] Coenrad J Fourie, Olaf Wetzstein, Thomas Ortlepp, and Jürgen Kunert. Three-dimensional multi-terminal superconductive integrated circuit inductance extraction. *Superconductor Science and Technology*, 24(12):125015, 2011.
- [26] Zheng Cui, John R. Kirtley, Yihua Wang, Philip A. Kratz, Aaron J. Rosenberg, Christopher A. Watson, Gerald W. Gibson, Mark B. Ketchen, and Kathryn A. Moler. Scanning squid sampler with 40-ps time resolution. *Review of Scientific Instruments*, 88(8):083703, 2017.
- [27] Leonardo Ranzani, Lafe Spietz, Zoya Popovic, and José Aumentado. Two-port microwave calibration at millikelvin temperatures. *Review of Scientific Instruments*, 84(3):034704, 2013.